



Electrosprayed MnO₂ on ZnO nanorods with atomic layer deposited TiO₂ layer for photoelectrocatalytic water splitting

Min-Woo Kim^{a,1}, Bhavana Joshi^{a,1}, Edmund Samuel^a, Hyunjun Seok^a, Ali Aldalbahi^b, Mohammed Almoqli^c, Mark T. Swihart^d, Sam S. Yoon^{a,*}

^a School of Mechanical Engineering, Korea University, Seoul, 02841, Republic of Korea

^b Department of Chemistry, College of Science, King Saud University, Riyadh, 11451, Saudi Arabia

^c Nuclear Science Research Institute, King Abdulaziz City for Science and Technology, Riyadh, 11442, Saudi Arabia

^d Department of Chemical & Biological Engineering and RENEW Institute, University at Buffalo, The State University of New York, Buffalo, NY, 14260-4200, USA

ARTICLE INFO

Keywords:

ZnO nanorods
Electrostatic spray
Water splitting
Photocatalyst
Ultrathin TiO₂

ABSTRACT

We have designed and produced a hierarchical photocatalyst for water splitting by first fabricating ZnO nanorods via a chemical bath deposition (CBD) process using ZnO seeds electrosprayed onto In-doped tin oxide (ITO), then electrospraying MnO₂ particles as a co-catalyst, and finally depositing an ultrathin passivation layer of TiO₂ via atomic layer deposition. These hierarchical photocatalysts exhibit excellent photoelectrochemical properties and reduced photocorrosion compared to materials without TiO₂ coating. Moreover, the MnO₂-garnished ZnO nanorods obtained at 550 °C deliver a 1.7-fold enhancement in photocurrent density (0.95 mA/cm²) at 1.2 V_{Ag/AgCl} in 0.5-M Na₂SO₃ solution compared to ZnO nanorods without MnO₂. We attribute improved photocurrent density to rapid charge transfer and charge separation at the ZnO–MnO₂ interface. This investigation illustrates a balanced design of a nanoarchitecture for photoelectrodes that favors formation of effective photoelectrocatalytic sites while improving stability for potential large-scale water splitting applications.

1. Introduction

Photoelectrochemical (PEC) water splitting is an environmentally benign process for converting solar energy into chemical energy. The hydrogen evolution reaction during PEC water splitting produces hydrogen that can be stored for later use as a clean energy source for fuel cells or combustion engines. The semiconducting metal oxides, such as ZnO, TiO₂, MnO₂, and Fe₂O₃ have been used as photoelectrodes in PEC water-splitting applications. These photoelectrode materials have excellent photoelectrocatalytic properties and are simple to fabricate into a photoanode. They are earth-abundant and of low cost. In addition to water splitting application, these metal oxides have also been used to degrade pollutants in water via photocatalysis [1–9].

Photoelectrodes of ZnO (3.37 eV) and TiO₂ (3.2 eV) have been widely used for PEC water splitting but they are only able to utilize the ultraviolet (UV) portion of the solar spectrum [10]. Thus, photocatalytic materials with activity in the visible light range (< 3 eV) such as MnO₂ and BiVO₄ are of great interest. These semiconducting materials absorb both UV and visible wavelengths to efficiently produce photogenerated electron-hole pairs to drive the oxygen and hydrogen

evolution reactions [1,4,9,11–15].

One- or two-dimensional (1D or 2D) nanostructures, such as nanorods, nanowires, nanosheets, and nanoflowers have been shown to exhibit excellent PEC performance compared to the corresponding bulk materials. The enhanced PEC performance of these nanostructures has been attributed to increased light absorption and faster transport of photogenerated charge carriers to reactive surface sites. Furthermore, these nanostructures exhibit high surface-to-volume ratios with open structures that provide short diffusion lengths in the electrolyte. All of these factors enhance PEC performance [15–17].

Nanostructure synthesis by techniques such as vapor–liquid–solid (VLS) deposition, chemical vapor deposition (CVD), and pulsed laser deposition (PLD) may not be scalable and thus not economically viable. In contrast, the growth of ZnO nanorods by facile chemical bath deposition and hydrothermal methods may offer a valuable practical route to scalable production. However, the direct growth of ZnO nanorods on indium-doped tin oxide (ITO) at low temperature is a challenge because of the mismatch in the lattice structures of ZnO and ITO. Pre-deposition of a ZnO seed layer on ITO reduces the activation barrier for ZnO nucleation and alleviates lattice strain to facilitate efficient

* Corresponding author.

E-mail address: skymoon@korea.ac.kr (S.S. Yoon).

¹ These authors have contributed equally.

growth of ZnO nanorods [18,19]. Although the ZnO nanorod morphology improves incident light absorbance [20,21], short charge-carrier lifetime and photocorrosion may continue to limit the water-splitting efficiency and stability [22–27]. Therefore, ZnO/MnO₂ heterostructures [28,29] have been introduced to enhance both visible light absorbance and charge carrier separation [9,16]. The band-transport mechanism of ZnO/MnO₂ is suitable for driving O₂ evolution at the photoanode surface with H₂ generation at the counter electrode (Pt) [4,29,30].

An ultrathin passivation layer of TiO₂ formed by atomic layer deposition (ALD) is an effective conformal coating to overcome the major limitation of ZnO's poor stability, as previously demonstrated by our group [31–33]. An ultrathin layer of TiO₂ prevents direct contact of the photoactive material with the electrolyte, ultimately reducing photocorrosion [34]. Moreover, TiO₂ over the active layer-forming interface results in reduced tunneling barrier and interfacial resistance [35]. The ultrathin TiO₂ allows holes from the photoactive material to reach the surface to participate in the oxygen evolution reaction in water splitting. Many reports have tested the effectiveness of passivation layers against photocorrosion, showing that stabilization characteristics may vary depending on the deposition technique used for the passivation layer [28,34,36,37].

Here, we demonstrate chemical bath growth of ZnO nanorods over an electrostatic spray deposited (ESD) ZnO seed layer on an ITO substrate, followed by deposition of MnO₂ nanoparticles on the ZnO nanorods via ESD. As a non-vacuum technique, ESD is facile and well known for ~100 % deposition efficiency (almost no loss of precursor solution in the deposition environment), good dispersion, uniformity, good wettability, and fine droplets. The high targeting accuracy of charged droplets towards the substrate is another special property of ESD [32,38,39]. When ESD was used for MnO₂ nanoparticle deposition, the nanoparticles were well distributed on the ZnO nanorods as a result of high targeting accuracy. The addition of MnO₂ increased the photocurrent response. The stability of the ZnO nanorods during PEC water splitting was significantly improved after ALD of an ultrathin TiO₂ passivation layer.

2. Experimental methods

2.1. Materials

Zinc acetate dihydrate (ZnAc, Zn(CH₃COO)₂·2H₂O, Sigma-Aldrich) and acetic acid (CH₃COOH, 99.7 %, Samchun Chemicals) were used for the ZnO seed layer coating. For ZnO nanorod growth, ZnAc and hexamethylenetetramine (HMT, C₆H₁₂N₄, Sigma-Aldrich) were mixed. To electrodeposit the MnO₂ nanoparticles, manganese(II) nitrate tetrahydrate (MnNT, Mn(NO₃)₂·4H₂O, Sigma-Aldrich) was mixed with acetic acid (CH₃COOH, 99.7 %, Samchun Chemicals).

2.2. ZnO nanorod chemical bath growth

The precursor solution for the ZnO seeding process was prepared by mixing 0.0275 g ZnAc with 10 mL acetic acid. Next, the ZnAc precursor solution was coated on ITO substrates by ESD for 20 min. The optimized ESD process parameters to obtain a stable cone jet are presented in Table 1. The Zn-seeded ITO substrates were then annealed at 350 °C for 30 min in air.

The ZnO nanorods were grown over the ZnO-seeded substrates by a facile CBD method. The precursor solution for the synthesis of ZnO nanorods was made by mixing 0.1-mM ZnAc and 0.1-mM HMT in deionized (DI) water followed by stirring for 24 h at room temperature. The ZnAc provided Zn while HMT functioned as a crystal modifier for nanorod growth. The ZnO-seeded films were soaked in the ZnAc/HMT solution for 30 min, during which the ZnO nanorods were grown via recrystallization of the ZnO seed layer and deposition of Zn²⁺ ions from ZnAc dissolution. The samples were then washed in DI water and dried

Table 1

ESD operating conditions of ZnO seeding and MnO₂ coating.

Items		Conditions
ZnO seeding	Substrate	Indium tin oxide (ITO) - coated glass
	Flow rate [μL/hr]	1200
	Applied voltage [kV]	12
	ITO substrate dimensions [cm ²]	2.5 × 2.0
	Distance nozzle to substrate [cm]	4.5
	Substrate temperature, [°C]	80
MnO ₂ coating	Substrate	ZnO nanorods films
	Flow rate [μL/hr]	800
	Applied voltage [kV]	10.3
	ITO substrate dimensions [cm ²]	2.5 × 2.0
	Distance nozzle to substrate [cm]	4.5
	Substrate temperature, [°C]	80

with Ar gas at room temperature. The schematic shown in Fig. 1a depicts the seed-layer deposition by ESD and the soaking of the annealed ZnO seed layer for transformation into ZnO nanorods.

2.3. MnO₂-garnished ZnO nanorods by ESD

The ZnO nanorods were further decorated with MnO₂ nanoparticles to enhance their PEC performance. For MnO₂ deposition by ESD, the precursor solution was prepared by dissolving 0.625 g MnNT in 10 mL acetic acid at room temperature. The vertically aligned ZnO nanorods were coated with the Mn precursor by ESD. The Mn solution deposition time was 5, 10, or 30 s. The Mn-decorated ZnO nanorods were then annealed at 550 °C for 30 min in air. The process parameters for Mn solution deposition by ESD are listed in Table 1. Annealing of MnO at 500–700 °C in air can yield Mn₂O₃ that might enhance the oxygen evolution reaction [40,41]. However, to preserve the ITO and to obtain the MnO₂ phase, the annealing temperature was restricted to 550 °C.

Finally, over the ZnO/MnO₂ nanorods, a thin layer of TiO₂ was deposited by ALD (Lucida™ D series ALD system, NCDtech, Korea) using titanium (IV) isopropoxide (EGchem) as the Ti precursor. Water vapor was provided for oxidation. The process conditions for the TiO₂ deposition by ALD are presented in Table 2. The deposition rate of TiO₂ was ~0.1 nm/cycle; thus, the thickness of the TiO₂ layer was controlled by changing the number of cycles (*n* indicates the number of cycles). Fig. 1b illustrates the effect of each material, where ZnO nanorods act as *n*-type semiconductors that generate electron-hole pairs for water splitting. The MnO₂ nanoparticles garnished over the ZnO nanorods enhance visible-light absorption and effective charge separation, thereby enhancing the PEC effect. The ultrathin TiO₂ film on the nanorods as a passivation layer prevents the photocorrosion of the nanorods in the presence of an electrolyte.

2.4. Film characterization

X-ray diffraction (XRD, D/max-2500, Rigaku, Japan) analysis was performed using Cu Kα radiation in the 2θ range 10–80° to identify the crystalline phases. The chemical states of the surface elements of the films were determined using X-ray photoelectron spectroscopy (XPS, X-TOOL, ULVAC-PHI). The morphologies of the films were observed using high-resolution scanning electron microscopy (HR-SEM, XL30 SFEG, Phillips Co., Holland) at 15 kV acceleration voltage. Transmission electron microscopy (TEM, JEM 2100 F, JEOL Inc.) was employed for in-depth morphological analysis of the samples. The TEM samples were prepared by the focused ion beam (FIB, 5 nA, LYRA3 XMH, TESCAN) technique to acquire cross-sectional views. Energy-dispersive X-ray

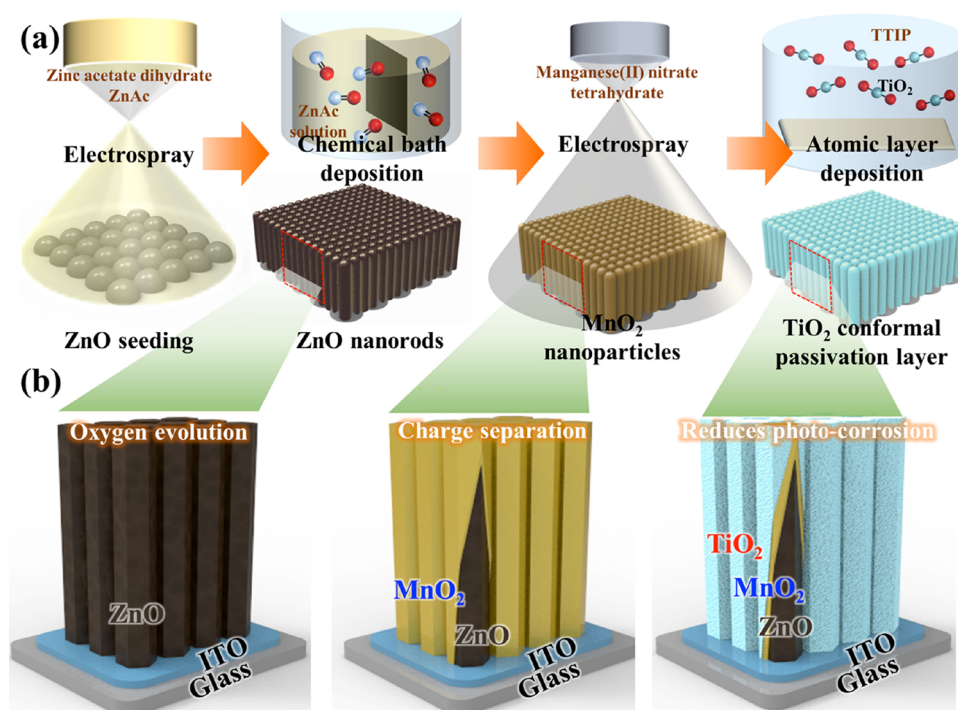


Fig. 1. (a) Schematic of the fabrication of ZnO/MnO₂/TiO₂ nanorods, and (b) illustration of the effect of each coated layer.

spectroscopy (EDS) coupled with TEM was also employed for elemental mapping. A UV–vis spectrometer (Optizen POP Mecasys Co. LTD, Korea) was used to measure the film absorbance.

2.5. Electrochemical characterization

To observe the PEC performance of the ZnO, ZnO/MnO₂, and ZnO/MnO₂/TiO₂ nanorod film photoelectrodes, the photocurrent density (PCD) values of the films were measured using a three-electrode setup. The photoelectrode film, Ag/AgCl, and a Pt wire were used as the working, reference, and counter electrode, respectively. A 0.5-M Na₂SO₄ solution (pH 7) was used as the electrolyte. To simulate sunlight (100 mW/cm²), we used a Xe arc lamp (Newport, Oriol Instruments, USA) equipped with an AM 1.5 filter. The dark current and photocurrent were measured by a potentiostat (VersaSTAT-3, Princeton Applied Research, USA) for linear sweep voltammetry and applied voltage range of -0.2 to 1.2 V (versus Ag/AgCl) at a scan rate of 10 mV/s. The PCD was also tested using a Na₂SO₃ hole-scavenging electrolyte. Mott–Schottky measurements were performed using the above-mentioned potentiostat and three-electrode setup in the voltage window from 0 to -1 V vs. Ag/AgCl.

3. Results and discussion

3.1. MnO₂-garnished ZnO nanorods passivated by TiO₂

The ZnO seed layer was prepared by ESD on ITO and analyzed by SEM as presented in Fig. 2a and b. The cross-sectional SEM image (Fig. 2a) shows a uniform ~ 10 -nm-thick layer of ZnO seeds deposited by ESD. The top view (Fig. 2b) shows that the ZnO-seed film consists of

aggregated particles of ~ 50 – 100 nm in size, whereas the low-magnification image in the inset shows uniformity over a larger area. This ZnO-seeded ITO substrate, when soaked in a solution of ZnAc/HMT, experiences growth of ZnO nanorods (see Fig. S1a) from the ZnO seed particles. The height of the ZnO nanorods is approximately 5 μ m, and their average diameter is ~ 100 nm. These vertically-oriented nanorods provide relatively long (axial) paths for light absorbance in combination with short (radial) transport distances to the interface with the electrolyte and large surface area for reaction. To improve visible light absorbance and charge separation, the ZnO nanorods were garnished with MnO₂ nanoparticles (see Fig. S1b). However, these small particles were not visible by SEM. Furthermore, when the TiO₂ ultrathin layer was applied, the morphology of the ZnO/MnO₂/TiO₂ nanorods appears unchanged in SEM because of the small amounts of MnO₂ and TiO₂ deposited as shown in Fig. 2c. The surface view of the ZnO/MnO₂/TiO₂ sample in Fig. 2d depicts nanorods of ~ 100 – 150 nm diameter and hexagonal cross-section. The inset image in Fig. 2d is a lower-magnification image that shows the uniformity of the nanorods over a larger area.

TEM analysis was performed to understand the morphology of the nanorods and the deposition of MnO₂ and TiO₂ over the nanorods. The side view in Fig. 3a shows ZnO nanorods with a diameter of ~ 80 nm. The elemental line profile in the inset of Fig. 3a shows the elemental distribution of Zn (brown) in the center and Mn (yellow) and Ti (blue) at the edges. The HR-TEM image in Fig. 3b depicts two sections; the center part highlighted in red is ZnO, and the edge, highlighted in yellow, depicts the presence of a different layer morphology that can be attributed to MnO₂/TiO₂ layers. The blue dashed part in the inset of Fig. 3b shows no particular lattice fringes, suggesting that the TiO₂ layer is amorphous. The lattice fringes are apparent in Fig. 3b and c,

Table 2
ALD processing conditions.

Coatings	Overall pressure [Torr]	Process temperature [°C]	Deposition rate [nm/cycle]	Number of cycles
TiO ₂	3×10^{-1}	200	0.1	10, 20, 50

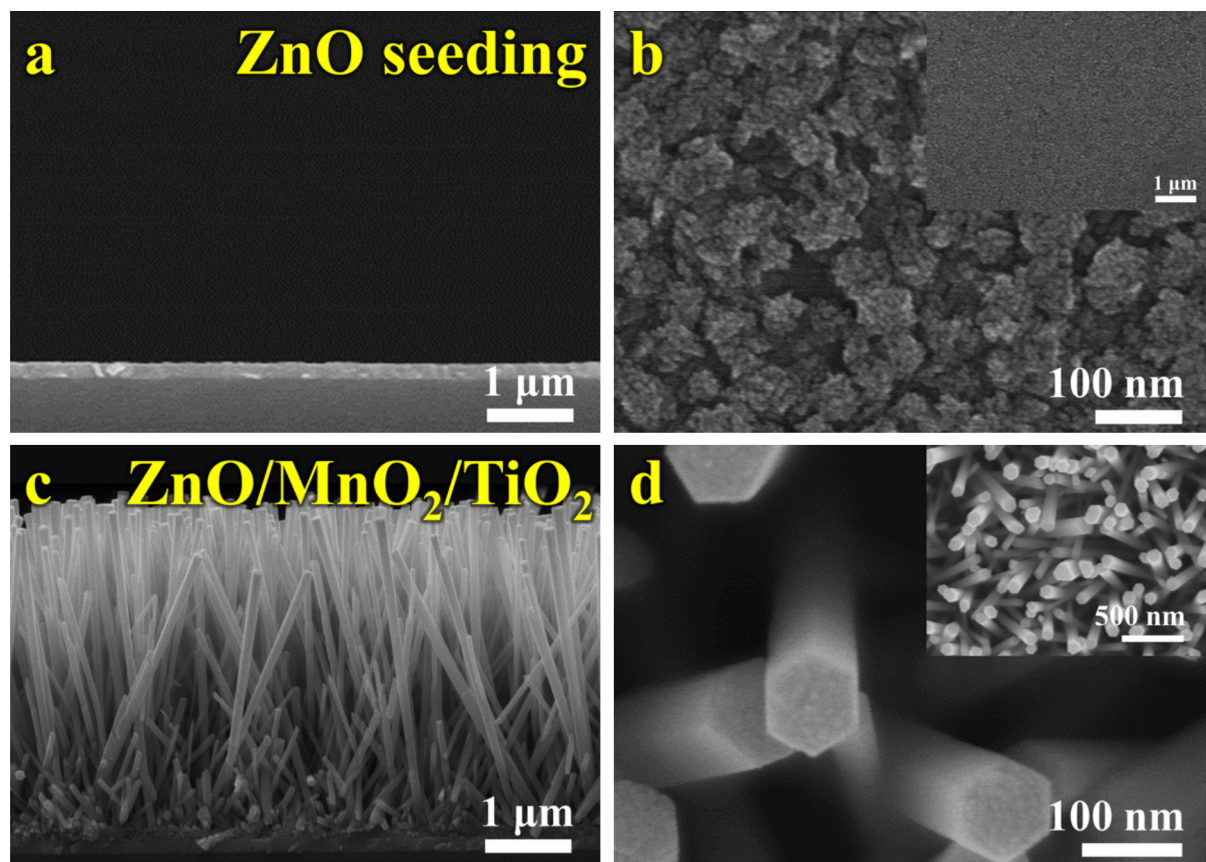


Fig. 2. SEM images: (a) cross-section view, and (b) top-view, with lower magnification inset of ZnO-seeded film, (c) cross-section view, and (d) top-view, with lower magnification inset, of ZnO/MnO₂/TiO₂ nanorod film.

where the d spacings of 0.26 and 0.20 nm correspond to the (100) and (101) planes, respectively, of ZnO [42,43]. The elemental mappings in Fig. 3d–f depict Zn, Mn, and Ti. The Zn mapping shows the structure of the nanorod, whereas the yellow and green dots of Mn and Ti confirms MnO₂ and TiO₂ deposition.

The XRD pattern of the ZnO/MnO₂/TiO₂ nanorods on ITO substrates is presented in Fig. 4a. The XRD pattern depicts a sharp diffraction peak at $2\theta = 34.4^\circ$, corresponding to the (002) plane of ZnO. The (002)-oriented ZnO nanorods are also called c -axis-oriented nanorods. This happens because HMT works as a capping agent over nonpolar facets of the wurtzite structure, preventing growth in other directions. Other peaks of wurtzite ZnO (JPCDS, No. 36-1451) at $2\theta = 31.2, 36.3, 47.6, 56.6, 62.9,$ and 67.9° are attributed to the (100), (101), (102), (110), (103), and (112) planes respectively [1,44]. Furthermore, no diffraction peaks associated with MnO₂ or TiO₂ are observed in the XRD pattern because of their smaller quantities, limited crystallinity, and/or small crystallite size. The diffraction peaks apparent in the XRD pattern at $2\theta = 20, 30, 35, 50,$ and 61° arise from the ITO substrate.

The XPS survey spectrum of the ZnO/MnO₂/TiO₂ nanorod film sample is presented in the supporting information (Fig. S2). The core XPS scans of Zn, Mn, and Ti from the ZnO/MnO₂/TiO₂ nanorod film are shown in Fig. 4b–d. The Zn 2p region (Fig. 4b) exhibits two sharp peaks centered at 1021.2 and 1044.2 eV, corresponding to Zn 2p_{3/2} and Zn 2p_{1/2}, respectively. The spin-orbit splitting energy of 22.6 eV indicates the presence of Zn as Zn²⁺ [44–47]. The Mn 2p spectrum in Fig. 4c shows Mn 2p_{3/2} and Mn 2p_{1/2} peaks at 643.9 eV and 654 eV, respectively, suggesting that Mn is present as MnO₂ in the composite. The spin-orbit splitting separation between the two Mn 2p peaks is 10.1 eV, which is slightly lower than the usual binding energy difference [29]. Fig. 4d shows the Ti 2p spectrum with peaks located at 458 eV and 463.8 eV, ascribed to the Ti 2p_{3/2} and Ti 2p_{1/2} orbitals, confirming the

presence of Ti in the Ti⁴⁺ state [48,49]. Moreover, the XPS-based concentrations of Zn and O atoms in ZnO/MnO₂/TiO₂ slightly decreased (see Table S1) relative to their concentrations in ZnO/MnO₂, accompanied by the appearance of Ti (~3.1%). The measured Mn content increased slightly from 7.9% to 8.1%, and the carbon concentration increased marginally from 1.4% to 1.9% as shown in Table S1, but we do not consider these marginal increases to be significant. Overall, the XPS-based surface concentration measurements demonstrate the successful deposition of MnO₂ and TiO₂ over the ZnO nanorods.

3.2. PEC performance

The absorbance spectra of five different samples (ZnO, ZnO/MnO₂, and ZnO/MnO₂ with 10, 20, and 50 cycles of TiO₂ coating) are presented in Fig. 5a. The absorbance of each sample was measured using a UV–vis spectrometer with a bare ITO glass substrate as the background reference. Fig. 5a clearly shows the increase in absorbance at visible wavelengths with the addition of MnO₂. The ZnO/MnO₂ nanorods with 10 cycles of TiO₂ exhibit a slight increase in absorbance, but for higher TiO₂ cycle numbers, the absorbance decreased gradually. It is important to note that the absorption edge of the ZnO/MnO₂ sample does not shift to a higher wavelength, possibly because of the low concentration of MnO₂. The optical bandgap energies determined from the linear part of the Tauc plot ($(\alpha h\nu)^2$ vs. $(h\nu)$) are shown in Fig. 5b. The bandgap energy of ZnO (3.3 eV) is as expected; the addition of MnO₂ nanoparticles slightly decreases the bandgap to 3.2 eV. The bandgap is further decreased to 3.1 eV with 10 cycles of TiO₂ coating; with further increase in the number of cycles, the bandgap increases. The bandgap decrease with the addition of 10 cycles of TiO₂ may be from the passivation of interfacial states as the concentrations of defects such as dangling bonds

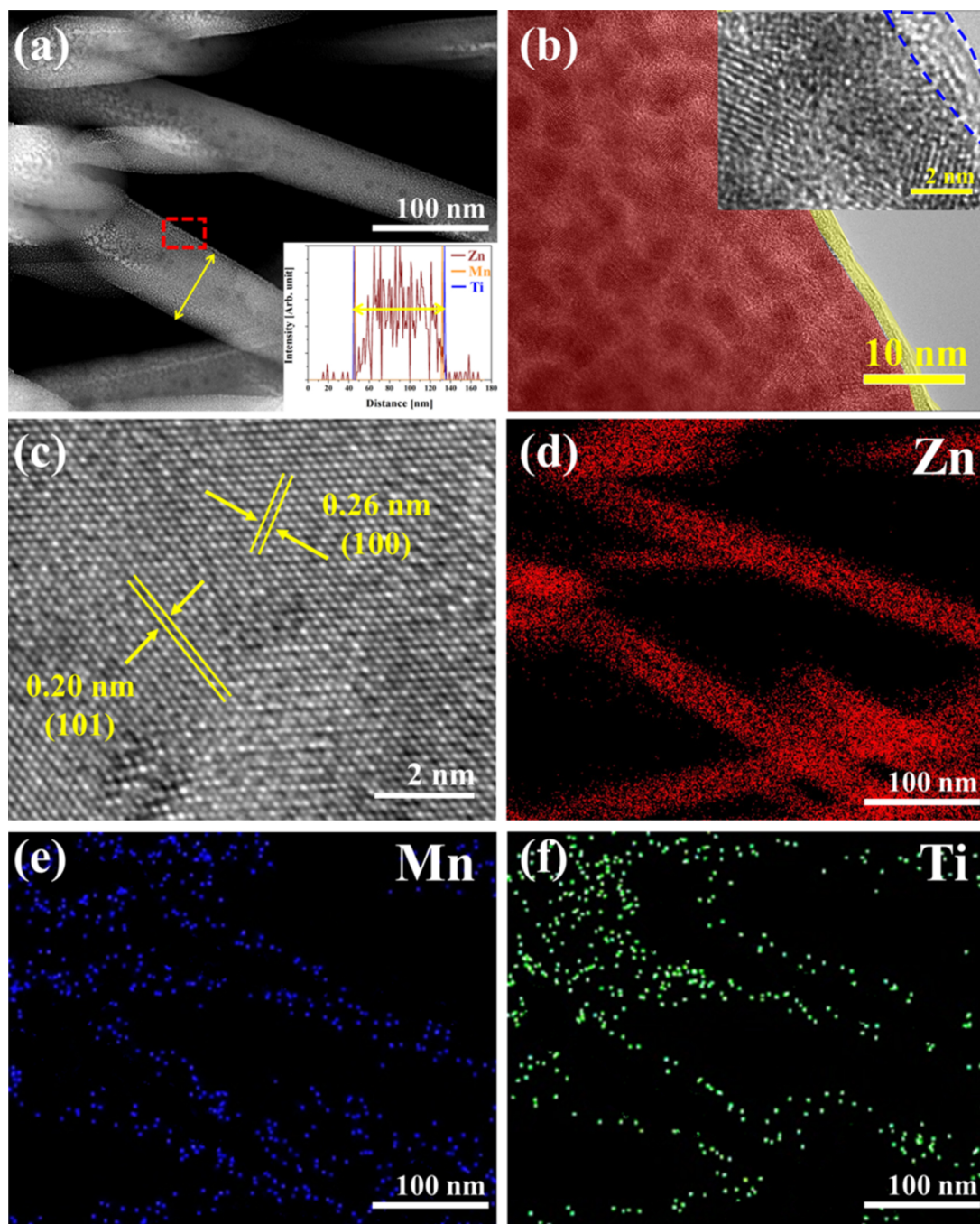


Fig. 3. (a) TEM image; inset: EDS line scan across ZnO/MnO₂/TiO₂ nanorod diameter as indicated by yellow arrow, (b, c) high-resolution TEM images of the inner area of the nanorod, (d–f) EDS maps showing Zn, Mn, and Ti of the ZnO/MnO₂/TiO₂ nanorods. (For interpretation of the references to colour in this figure legend, the reader is referred to the web version of this article).

are reduced with higher number of ALD cycles. The band alignment for ZnO/MnO₂/TiO₂ is as shown in Fig. S3. As the conduction band maximum of MnO₂ (0.57 eV vs. normal hydrogen electrode (NHE)) is positive compared to that of TiO₂ the electrons easily hop from TiO₂ to MnO₂. Thus, the presence of a TiO₂ overlayer favors charge-separation.

To observe the impact of MnO₂ and TiO₂ over the ZnO nanorod, the photocatalytic degradation of methylene blue (MB) was studied using simulated sunlight from a Xe arc lamp with a 450-nm long-pass filter that allows visible wavelength transmission but prevents UV transmission. The films were soaked in a MB solution for 10 min under illumination. The concentration of MB was measured before (C_0) and after illumination (C). The results of the MB solution degradation for each film are shown in Fig. 5c. In the case of ZnO nanorods, the MB

degradation was only 30 %, but it reached 91 % with MnO₂ garnished over the ZnO nanorods. The addition of TiO₂ slightly decreased the MB degradation rate. Nonetheless, the impact of MnO₂ is evident in the presence of TiO₂; the extent of MB degradation remained much higher than that with the pristine ZnO nanorods.

The transient responses of the samples were measured in Na₂SO₄ electrolyte at different potentials, as presented in Fig. 5d. During the linear-sweep voltammetry (LSV), illumination was blocked at consistent intervals. At voltages exceeding 0.4 V, the sudden rise and fall in the PCD under illumination and in the absence of illumination, respectively, indicate that all samples exhibit fast charge-transfer characteristics and excellent photocatalytic activity and are thus suitable for further PEC testing.

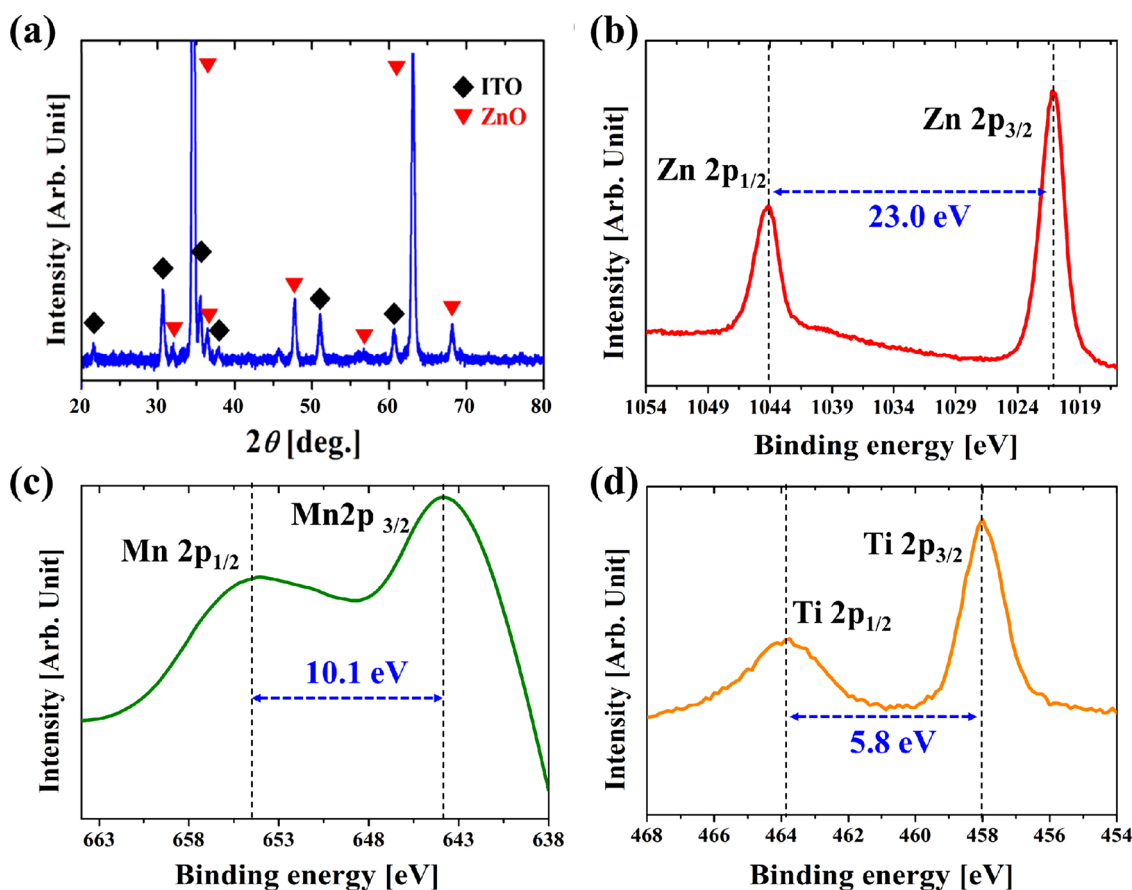


Fig. 4. (a) XRD pattern, and (b–d) XPS spectra (b) Zn 2p, (c) Mn 2p, and (d) Ti 2p for ZnO/MnO₂/TiO₂ nanorods.

The PCDs measured using LSV for ZnO nanorods (0 s) and 5-, 10-, and 30-s MnO₂-garnished ZnO nanorods in Na₂SO₄ electrolyte are presented in Fig. 6a. The PCD values are the highest in the positive potential region, indicating that the fabricated electrodes are n-type in nature and work as anodes for oxygen generation. In dark conditions, *i.e.*, without illumination, the current density of all samples is zero. The PCD values observed under illumination indicate that charge carrier generation is increased by the incident photons, which significantly contributes to water splitting. The PCD of the pure ZnO nanorods is 0.1 mA/cm² at 1.2 V vs. Ag/AgCl. On the other hand, 5 and 10 s of ESD MnO₂ garnishing of the ZnO nanorods yield PCD increases to 0.4 and 0.55 mA/cm², respectively. However, for a longer MnO₂ ESD time (*i.e.*, 30 s), the PCD decreased.

Next, we conducted experiments using Na₂SO₃ as an electrolyte, in which sulfite acts as a sacrificial agent (hole scavenger) favoring sulfite oxidation over water oxidation. The PCDs of the same samples measured in the Na₂SO₃ electrolyte are presented in Fig. 6b. As an effect of the sacrificial sulfite, the onset potential is shifted to lower potential (0 V_{Ag/AgCl}) compared to that in Na₂SO₄ (0.2 V_{Ag/AgCl}) in all cases. Additionally, the PCD is almost doubled (0.95 mA/cm²) relative to the PCD in Na₂SO₄ (0.55 mA/cm²) for the MnO₂-garnished ZnO nanorods. Furthermore, with a passivation layer from 10 cycles of ALD of TiO₂ on ZnO/MnO₂, the PCD is comparable to that from ZnO/MnO₂ nanorods. Here, the hole-scavenging Na₂SO₃ electrolyte ensures that the oxidation at the photoanode surface is faster, and the PEC data reveals the efficient charge-carrier generation and separation rates in the heterostructured ZnO/MnO₂.

The effect of the TiO₂ coating on PEC performance was tested in Na₂SO₄, as shown in Fig. 6c. For all TiO₂ coatings, the ZnO nanorods are garnished with MnO₂ for 10 s, the optimized condition to maximize the PCD value, as per Fig. 6a and b. The PCD of the ZnO/MnO₂ nanorods

was 0.55 mA/cm² at 1.2 V_{Ag/AgCl}, as represented by the red dashed line in Fig. 6c. The ALD-coated thin layers of TiO₂ on ZnO/MnO₂ nanorods were expected to improve the electrical and optical properties of the samples. However, the presence of the TiO₂ layer does not improve the PCD. For 10 cycles of TiO₂ deposition over the ZnO/MnO₂ nanorods, the PCD is slightly decreased (0.5 mA/cm²), and it is further decreased to 0.35 mA/cm² for 50 cycles of TiO₂ deposition. The stability of samples in Na₂SO₄ at a potential of 1.2 V_{Ag/AgCl} for 1000s was measured by chronoamperometry, as presented in the supporting information (Fig. S4). The PCDs of the ZnO, ZnO/MnO₂, and 10-, 20-, and 50-cycle TiO₂-coated ZnO/MnO₂ are 0.45, 0.6, and 0.5, 0.38, and 0.35 mA/cm², respectively, at *t* = 0 s (see Fig. 6d). After 1000s, the PCDs are decreased by 50 and 54 % for the ZnO and ZnO/MnO₂ nanorods (see retention values in Fig. 6d). However, the passivation layers of TiO₂ clearly improve the stabilities of the ZnO/MnO₂ nanorods coated with 10, 20, and 50 cycles of TiO₂. Almost 80 % of the PCD is retained after 1000 s, indicating that the presence of TiO₂ is essential for stability enhancement of ZnO-based photoanodes. As noted earlier, the TiO₂ coating eliminated direct contact between the photoactive electrode and the electrolyte, thus suppressing the photocorrosion of the ZnO nanorods.

H₂ and O₂ evolution measurements were then performed for the photoelectrochemical reaction. Oxygen evolution occurs at the photoelectrode, while H₂ is released at the Pt plate counterelectrode. The measurement of O₂ and H₂ production carried out in the photoelectrochemical cell is as presented in supporting media Movie S1. The production of O₂ and H₂ occurs in separate chambers. The scale is presented at the top of the PEC cell to measure the respective volumes of O₂ and H₂ gases. The isolated O₂ and H₂ gas measurements show the volume of H₂ to be 4.9 mL and that of O₂ to be 2.2 mL; see Movie S1). The greater than 2:1 ratio of H₂ to O₂ may reflect the fact that some O₂

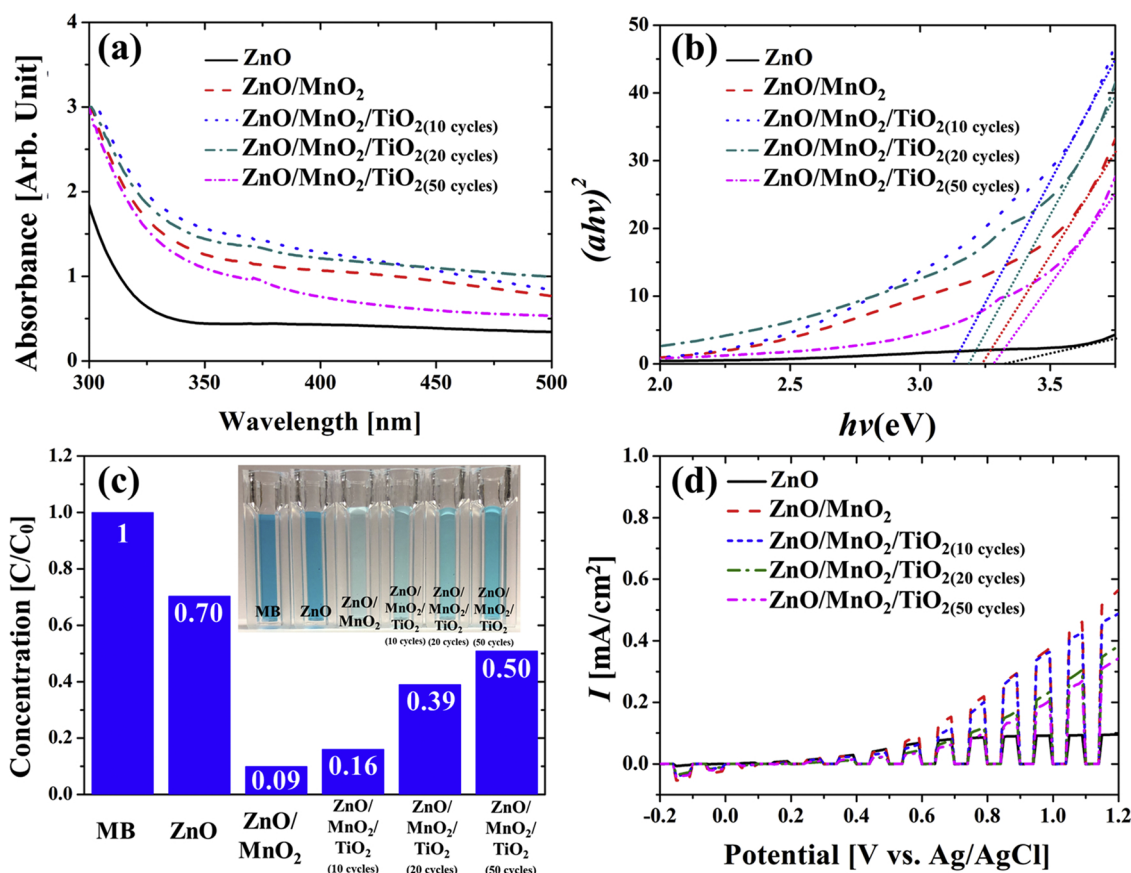


Fig. 5. (a) Absorbance, (b) Tauc plot, (c) photocatalytic dye degradation, and (d) transient photoresponses of pristine ZnO nanorod, ZnO/MnO₂, and ZnO/MnO₂ with 10, 20, and 50 ALD cycles of TiO₂ coating.

produced remains dissolved in the electrolyte. The Faradaic efficiency (η_{O_2}) of O₂ production can be estimated from the measured volume of oxygen. The Faradaic efficiency is defined as the ratio of charge transferred during the O₂ evolution to the total charge consumed during the static photoelectrochemical measurements. The Faradaic efficiency for O₂ evolution at the photoelectrode during PEC water splitting can be determined using Eq. (1) as follows: [50]

$$\eta_{O_2} = \frac{V_E}{V_T} = \frac{V_E}{(Q \cdot V_m) / (4 \cdot F)} \quad (1)$$

Where V_E is the measured volume of collected O₂ from PEC water splitting, V_T is theoretical volume of O₂, Q is the charge summation of the photoelectrode, V_m is molar volume of gas (24.1 L mol⁻¹, 293 K, 101 kPa) and F is the Faraday constant. By using the constant values and charge summation for the PEC water splitting duration of 60 min, the estimated value of η_{O_2} is 58.7 %. The high Faradaic efficiency can be attributed to the stable and improved photocurrent performance of the photoanode due to the presence of MnO₂ and TiO₂.

The textural properties of nanostructures play an important role in the water-splitting process. Thus, N₂ adsorption-desorption analysis was performed for the ZnO nanorods. Fig. S5a and b depict the N₂ adsorption-desorption isotherm and pore size distribution, respectively. The rise in the isotherm (Fig. S5a) at a partial pressure > 0.8 along with some hysteresis during desorption confirms the presence of mesopores. The Barrett-Joyner-Halenda (BJH) pore size distribution in Fig. S5b shows a wide peak centered at 25 nm and the Brunauer-Emmett-Teller (BET) surface area is 22.8 m² g⁻¹.

Mott-Schottky (MS) plots are useful to investigate the concentration of free carriers in photoelectrodes. These measurements were performed in 0.5-M Na₂SO₄ as an electrolyte for ZnO, ZnO/MnO₂, and ZnO/MnO₂ coated with TiO₂ by 10, 20, and 50 cycles of ALD to

estimate the donor concentrations. The MS measurements were performed in the absence of illumination with 10 mV amplitude modulation at a fixed frequency of 1000 Hz. The Mott-Schottky plots in Fig. 7a follow the expected relationship for an ideal semiconductor:

$$\frac{1}{C_{sc}^2} = \left(\frac{2}{e\epsilon\epsilon_0 N_D} \right) \left(\frac{E - E_{fb} - kT}{e} \right) \quad (2)$$

where E is the conduction band potential (V), E_{fb} is the flat-band potential (V), k is the Boltzmann constant, T is the absolute temperature (K), e is the electron charge (C), ϵ is the relative permittivity, ϵ_0 is the permittivity of vacuum, N_D is the donor concentration per unit volume (cm⁻³), and C_{sc} is the surface charge capacitance (F cm⁻²). The Mott-Schottky plot-derived donor concentrations are as shown in Fig. 7b, revealing that addition of MnO₂ increases the electron concentration. Although the bare ZnO has a reasonable electron concentration, the fast recombination of electron-hole pairs (see Fig. 7d), and lower rate of hole transfer to electrolyte result in lower PCD values (see Fig. 6). The rate of this electron-hole recombination is reduced through band bending associated with the Mott-Schottky heterojunction [51]. Thus, the presence of MnO₂ over ZnO causes slower recombination as the electron flow occurs through the heterojunction interface [52]. Consequently, it increases the surface charge capacitance and leads to enhanced charge separation due to band bending as shown in Fig. 7e. The electron concentrations for ZnO, ZnO/MnO₂, and 10-, 20-, and 50-cycle TiO₂-coated ZnO/MnO₂ are 8.2, 8.6, and 7.7, 4.6, and 4.6 × 10¹⁷ cm⁻³, respectively.

With addition of the TiO₂ passivation layers, the donor concentration decreases. The decreased electron concentration caused by the passivation layer is consistent with the PCD response, as shown in Fig. 6c. The reduced donor concentration could be due to lowering of E_{fb} and space charge layer width (W_{SCL}) as depicted in Table 3. The

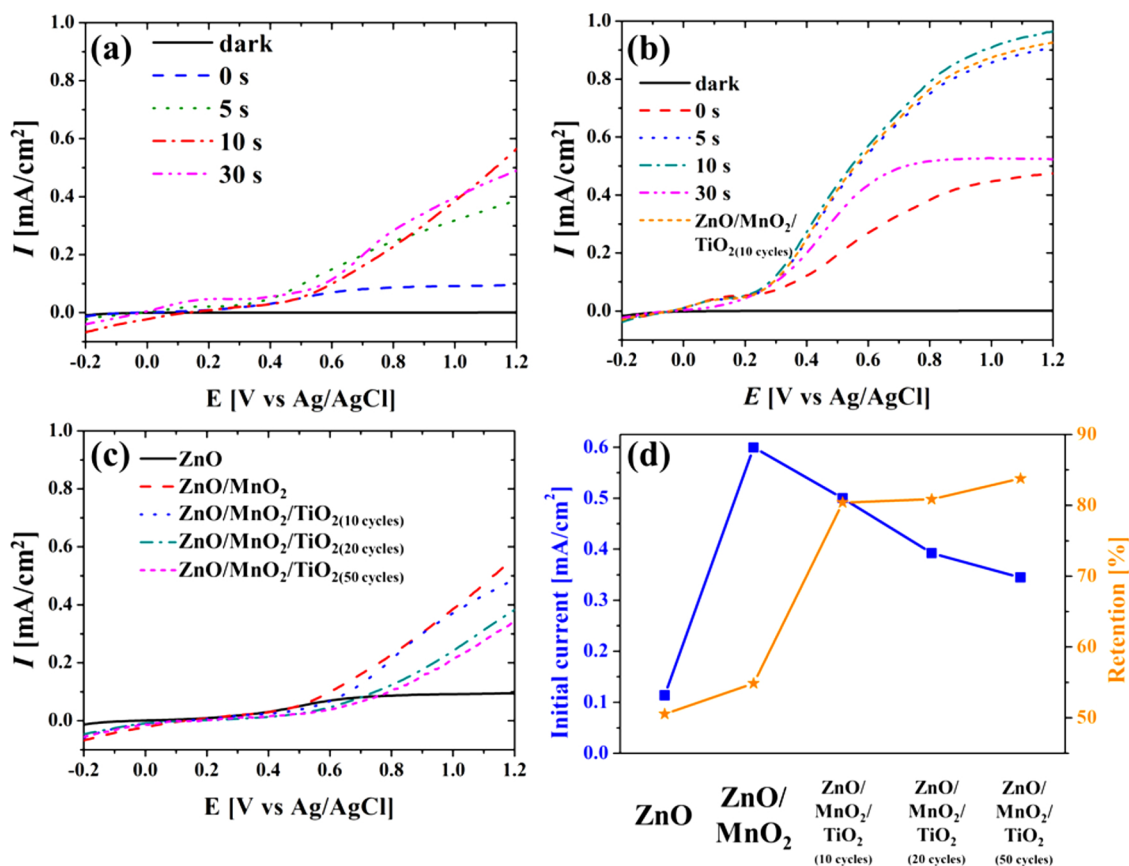


Fig. 6. The change of PCD upon increasing Mn spraying time in (a) Na₂SO₄ electrolyte and (b) Na₂SO₃ electrolyte. (c) PCD, and (d) stability (after 1000s at 1.2 V_{Ag/AgCl}) of ZnO, ZnO/MnO₂, and ZnO/MnO₂/TiO₂ with different numbers of ALD cycles for TiO₂ deposition.

lower W_{SCL} of ZnO promotes rapid recombination of electron-hole pairs [53,54]. However, the higher width of the space charge layer at the interface of the heterojunction reduces the recombination rate [55]. The net result is that TiO₂ as passivation layer provides stability (see Fig. 6d) and enhanced PCD (see Fig. 6c). The W_{SCL} can be calculated from the following relation [51,56].

$$W_{SCL} = \sqrt{\frac{2\epsilon\epsilon_0}{eND}(E - E_{fb} - \kappa T/e_0)} \quad (3)$$

where all the symbols have the conventional meanings as described for Eq. (2).

The PEC mechanism for PCD response is illustrated in Fig. 7d–f. The schematic in Fig. 7c shows the ZnO nanorods conformally coated with MnO₂ and TiO₂. ZnO suffers from rapid recombination under illumination (see Fig. 7d), which limits the photoelectrochemical performance and water splitting capability. The MnO₂ and TiO₂ coatings are very thin and the major PEC excitation of electrons and holes still occurs in the ZnO nanorods, rather than in these thin layers. However, these layers help to reduce recombination within ZnO. MnO₂, being mesoporous, allows permeation of electrolytic ions to the ZnO nanorods while prolonging the charge separation and serving as a co-catalyst; therefore, an enhanced PCD was observed for the ZnO/MnO₂ case (see Fig. 6b–c). The ZnO/MnO₂ had a larger W_{SCL} and increased upward band bending, which promotes the charge separation and simultaneously increases the photocurrent (see Figs. 7e and 6). However, to provide stability, conformal TiO₂ passivation layers (see Fig. 7d) are also needed. The presence of TiO₂ improves the charge separation at the surface of the active sites and enhances water oxidation during the PEC process. Moreover, the overlayer of TiO₂ provides holes at the electrode–electrolyte interface, and reduces the photocorrosion of ZnO/

MnO₂. The presence of the MnO₂ layer between ZnO and TiO₂ facilitates the hole transport across the interfaces so that holes are captured by the TiO₂ layer. Thus, the TiO₂ overlayer acts as a charge-storage zone and ultimately injects the photogenerated holes into the electrolyte [57]. However, increasing the thickness of the TiO₂ overlayer (with higher number of ALD deposition cycles) may increase the depletion region that then limits PCD as observed from Fig. 6. Under an applied voltage, the photo-generated electrons move toward the ITO regardless of staggered band alignment (as shown Fig. S3), but if the TiO₂ layer is too thick, it becomes a barrier to charge transport to the electrolyte. TiO₂ has a valence band maximum (VBM) potential of 2.91 eV vs NHE and its conduction band maximum (CBM) potential is -0.29 eV vs. NHE. The VBM of TiO₂ is more positive than that of MnO₂ or ZnO, so it may act as a tunneling barrier for holes. The CBM of TiO₂ (-0.29 eV vs. NHE) is more positive than ZnO (-0.73 eV vs. NHE) and negative compared to that of MnO₂ (0.57 eV vs. NHE), but in operation, photogenerated electrons move away from TiO₂ toward ZnO, so this may have little effect [58].

4. Conclusion

In summary, *c*-axis-oriented ZnO nanorods garnished with MnO₂ nanoparticles and passivated by TiO₂ were fabricated using CBD methods, ESD, and ALD, respectively. The MnO₂ deposition time and TiO₂ film thicknesses were optimized to achieve enhanced and stable PEC performance. The garnishing of MnO₂ over the ZnO nanorods increased the PCD from 0.49 to 0.96 mA/cm², almost a factor of two, in the hole-scavenging Na₂SO₃ electrolyte. In addition, the ZnO/MnO₂ nanorods with ALD coatings of TiO₂ exhibited excellent PCD retention of $\sim 80\%$ after 1000s of reaction, compared to that of pristine ZnO (50

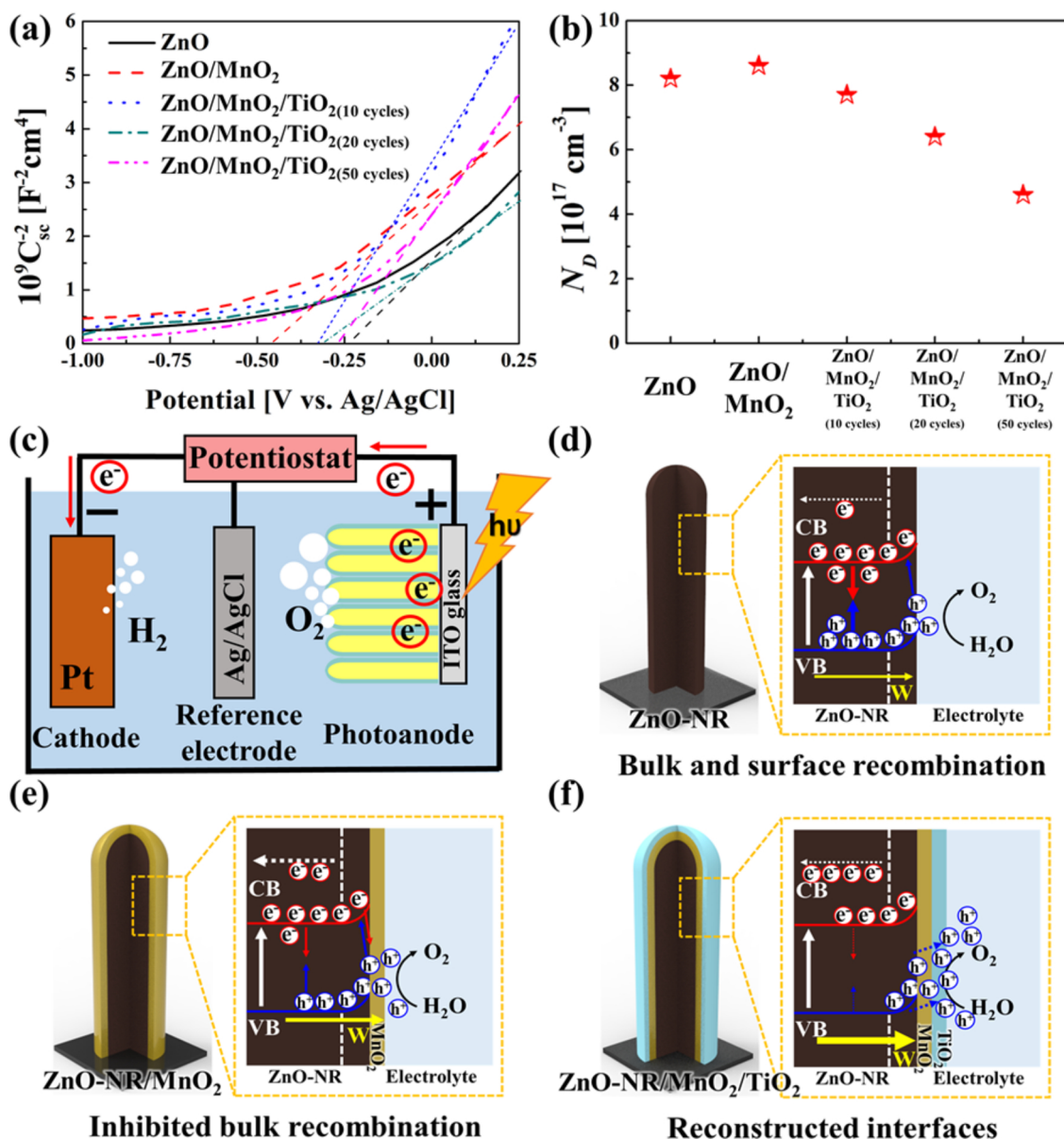


Fig. 7. (a) Mott-Schottky plot, and (b) electron concentrations (N_D) for various photoelectrodes. (c) A schematic of the three-electrode PEC system and (d-f) schematics illustrating (d) the mechanism of photocatalysis and the effects of (e) MnO₂ to promote charge separation and (f) TiO₂ as a passivation layer.

Table 3

Flat band potential and space charge layer width (W_{SCL}).

Samples	V_{fb} (V_{RHE})	W_{SCL} (nm)
ZnO	0.24	9.1
ZnO/MnO ₂	0.44	10.6
ZnO/MnO ₂ /TiO ₂ (10)	0.34	9.7
ZnO/MnO ₂ /TiO ₂ (20)	0.3	8.8
ZnO/MnO ₂ /TiO ₂ (50)	0.26	8.3

% or ZnO/MnO₂ (54 %). Mott-Schottky analysis depicted faster charge transport in the presence of the TiO₂ coating. Additionally, the high donor concentration (of $4-9 \times 10^{17} cm^{-3}$) for the photoelectrodes validated their superior PEC performance. Furthermore, MnO₂-garnished ZnO nanorods showed suitability for photocatalytic wastewater treatment, based on MB dye degradation studies.

Declaration of Competing Interest

The authors declare that they have no known competing financial interests or personal relationships that could have appeared to influence the work reported in this paper.

Acknowledgement

This research was supported by the Technology Development Program to Solve Climate Changes of the National Research Foundation (NRF) funded by the Ministry of Science, ICT & Future Planning, Republic of Korea (NRF-2016M1A2A2936760) and (NRF-2013R1A5A1073861). This research is also funded by King Saud University, Riyadh, Saudi Arabia, Researchers Supporting Project Number (RSP-2019/30).

Appendix A. Supplementary data

Supplementary material related to this article can be found, in the online version, at doi:<https://doi.org/10.1016/j.apcatb.2020.118928>.

References

- Z. Yu, H. Moussa, M. Liu, R. Schneider, W. Wang, M. Moliere, H. Liao, Development of photocatalytically active heterostructured MnO/ZnO and CuO/ZnO films via solution precursor plasma spray process, *Surf. Coat. Technol.* 371 (2019) 107–116.
- A.Y. Shan, T.I.M. Ghazi, S.A. Rashid, Immobilisation of titanium dioxide onto supporting materials in heterogeneous photocatalysis: a review, *Appl. Catal. A Gen.* 389 (2010) 1–8.
- P. Chen, G. Lee, S. Davies, S. Masten, R. Amutha, J. Wu, Hydrothermal synthesis of coral-like Au/ZnO catalyst and photocatalytic degradation of Orange II dye, *Mater. Res. Bull.* 48 (2013) 2375–2382.
- H. Peng, P.F. Ndione, D.S. Ginley, A. Zakutayev, S. Lany, Design of semiconducting tetrahedral $Mn_{1-x}Zn_xO$ alloys and their application to solar water splitting, *Phys. Rev. X* 5 (2015) 021016.
- D.C. Look, Recent advances in ZnO materials and devices, *Mater. Sci. Eng. B* 80 (2001) 383–387.
- Y. Yang, Y. Li, L. Zhu, H. He, L. Hu, J. Huang, F. Hu, B. He, Z. Ye, Shape control of colloidal Mn doped ZnO nanocrystals and their visible light photocatalytic properties, *Nanoscale* 5 (2013) 10461–10471.
- Z. Yi, J. Ye, N. Kikugawa, T. Kako, S. Ouyang, H. Stuart-Williams, H. Yang, J. Cao, W. Luo, Z. Li, An orthophosphate semiconductor with photooxidation properties under visible-light irradiation, *Nat. Mater.* 9 (2010) 559–564.
- P. Li, Z. Wei, T. Wu, Q. Peng, Y. Li, Au–ZnO hybrid nanopyrramids and their photocatalytic properties, *J. Am. Chem. Soc.* 133 (2011) 5660–5663.
- M. Shekofteh-Gohari, A. Habibi-Yangjeh, M. Abitorabi, A. Rouhi, Magnetically separable nanocomposites based on ZnO and their applications in photocatalytic processes: a review, *Crit. Rev. Environ. Sci. Technol.* 48 (2018) 806–857.
- A. Akhundi, A. Habibi-Yangjeh, M. Abitorabi, S. Rahim Pouran, Review on photocatalytic conversion of carbon dioxide to value-added compounds and renewable fuels by graphitic carbon nitride-based photocatalysts, *Catal. Rev.* 61 (2019) 595–628.
- R. Saravanan, S. Karthikeyan, V. Gupta, G. Sekaran, V. Narayanan, A. Stephen, Enhanced photocatalytic activity of ZnO/CuO nanocomposite for the degradation of textile dye on visible light illumination, *Mater. Sci. Eng. C* 33 (2013) 91–98.
- F. Achouri, S. Corbel, L. Balan, K. Mozet, E. Giro, G. Medjahdi, M.B. Said, A. Ghrabi, R. Schneider, Porous Mn-doped ZnO nanoparticles for enhanced solar and visible light photocatalysis, *Mater. Des.* 101 (2016) 309–316.
- A. Bosman, H. Van Daal, Small-polaron versus band conduction in some transition-metal oxides, *Adv. Phys.* 19 (1970) 1–117.
- M. Mousavi, A. Habibi-Yangjeh, S.R. Pouran, Review on magnetically separable graphitic carbon nitride-based nanocomposites as promising visible-light-driven photocatalysts, *J. Mater. Sci. - Mater. Electron.* 29 (2018) 1719–1747.
- M. Pirhashemi, A. Habibi-Yangjeh, S.R. Pouran, Review on the criteria anticipated for the fabrication of highly efficient ZnO-based visible-light-driven photocatalysts, *J. Ind. Eng. Chem.* 62 (2018) 1–25.
- Y. Yang, C. Zhang, D. Huang, G. Zeng, J. Huang, C. Lai, C. Zhou, W. Wang, H. Guo, W. Xue, Boron nitride quantum dots decorated ultrathin porous $g-C_3N_4$: intensified exciton dissociation and charge transfer for promoting visible-light-driven molecular oxygen activation, *Appl. Catal. B* 245 (2019) 87–99.
- H. Yi, M. Yan, D. Huang, G. Zeng, C. Lai, M. Li, X. Huo, L. Qin, S. Liu, X. Liu, Synergistic effect of artificial enzyme and 2D nano-structured Bi_2WO_6 for eco-friendly and efficient biomimetic photocatalysis, *Appl. Catal. B* 250 (2019) 52–62.
- W. Khan, H. Ajmal, F. Khan, N. Huda, S.-D. Kim, Induced photonic response of ZnO nanorods grown on oxygen plasma-treated seed crystallites, *Nanomaterials* 8 (2018) 371.
- E. Pourshaban, H. Abdizadeh, M.R. Golobostanfard, ZnO nanorods array synthesized by chemical bath deposition: effect of seed layer sol concentration, *Procedia Mater. Sci.* 11 (2015) 352–358.
- K. Davis, R. Yarbrough, M. Froeschle, J. White, H. Rathnayake, Band gap engineered zinc oxide nanostructures via a sol-gel synthesis of solvent driven shape-controlled crystal growth, *RSC Adv.* 9 (2019) 14638–14648.
- H.S. Jo, E. Samuel, H.-J. Kwon, B. Joshi, M.-W. Kim, T.-G. Kim, M.T. Swihart, S.S. Yoon, Highly flexible transparent substrate-free photoanodes using ZnO nanowires on nickel microfibers, *Chem. Eng. J.* 363 (2019) 13–22.
- K. Mageshwari, D. Nataraj, T. Pal, R. Sathyamoorthy, J. Park, Improved photocatalytic activity of ZnO coupled CuO nanocomposites synthesized by reflux condensation method, *J. Alloys. Compd.* 625 (2015) 362–370.
- P. Sathishkumar, R. Sweena, J.J. Wu, S. Anandan, Synthesis of CuO-ZnO nanophotocatalyst for visible light assisted degradation of a textile dye in aqueous solution, *Chem. Eng. J.* 171 (2011) 136–140.
- L. Xu, Y. Zhou, Z. Wu, G. Zheng, J. He, Y. Zhou, Improved photocatalytic activity of nanocrystalline ZnO by coupling with CuO, *J. Phys. Chem. Solids* 106 (2017) 29–36.
- D. Chen, H. Zhang, S. Hu, J. Li, Preparation and enhanced photoelectrochemical performance of coupled bi-component ZnO–TiO₂ nanocomposites, *J. Phys. Chem. A* 112 (2008) 117–122.
- B. Sambandam, R.J.V. Michael, P.T. Manoharan, Oxygen vacancies and intense luminescence in manganese loaded ZnO microflowers for visible light water splitting, *Nanoscale* 7 (2015) 13935–13942.
- S. Marthia, K.H. Reddy, K. Parida, Fabrication of In_2O_3 modified ZnO for enhancing stability, optical behaviour, electronic properties and photocatalytic activity for hydrogen production under visible light, *J. Mater. Chem. A Mater.* 2 (2014) 3621–3631.
- N.C. Strandwitz, D.J. Comstock, R.L. Grimm, A.C. Nichols-Nieler, J. Elam, N.S. Lewis, Photoelectrochemical behavior of n-type Si (100) electrodes coated with thin films of manganese oxide grown by atomic layer deposition, *J. Phys. Chem. A* 117 (2013) 4931–4936.
- D. Barreca, F. Gri, A. Gasparotto, G. Carraro, L. Bigiani, T. Altantzi, B. Žener, U.L. Štangar, B. Alessi, D.B. Padmanaban, Multi-functional MnO₂ nanomaterials for photo-activated applications by a plasma-assisted fabrication route, *Nanoscale* 11 (2019) 98–108.
- K.M. Nam, Y.-I. Kim, Y. Jo, S.M. Lee, B.G. Kim, R. Choi, S.-I. Choi, H. Song, J.T. Park, New crystal structure: synthesis and characterization of hexagonal wurtzite MnO, *J. Am. Chem. Soc.* 134 (2012) 8392–8395.
- T.-G. Kim, B. Joshi, C.-W. Park, E. Samuel, M.-W. Kim, M.T. Swihart, S.S. Yoon, Supersonically sprayed iron oxide nanoparticles with atomic-layer-deposited ZnO/TiO₂ layers for solar water splitting, *J. Alloys. Compd.* 798 (2019) 35–44.
- M.-W. Kim, K. Kim, T.Y. Ohm, H. Yoon, B. Joshi, E. Samuel, M.T. Swihart, S.K. Choi, H. Park, S.S. Yoon, Electrospayed BiVO₄ nanopillars coated with atomic-layer-deposited ZnO/TiO₂ as highly efficient photoanodes for solar water splitting, *Chem. Eng. J.* 333 (2018) 721–729.
- M.-w. Kim, H. Yoon, T.Y. Ohm, H.S. Jo, S. An, S.K. Choi, H. Park, S.S. Al-Deyab, B.K. Min, M.T. Swihart, S.S. Yoon, Nanotextured cupric oxide nanofibers coated with atomic layer deposited ZnO-TiO₂ as highly efficient photocathodes, *Appl. Catal. B* 201 (2017) 479–485.
- M.F. Lichterman, A.I. Carim, M.T. McDowell, S. Hu, H.B. Gray, B.S. Brunschwig, N.S. Lewis, Stabilization of n-cadmium telluride photoanodes for water oxidation to O₂ (g) in aqueous alkaline electrolytes using amorphous TiO₂ films formed by atomic-layer deposition, *Energy Environ. Sci.* 7 (2014) 3334–3337.
- D. Eisenberg, H.S. Ahn, A.J. Bard, Enhanced photoelectrochemical water oxidation on bismuth vanadate by electrodeposition of amorphous titanium dioxide, *J. Am. Chem. Soc.* 136 (2014) 14011–14014.
- B. Seger, D.S. Tilley, T. Pedersen, P.C. Vesborg, O. Hansen, M. Grätzel, I. Chorkendorff, Silicon protected with atomic layer deposited TiO₂: durability studies of photocathodic H₂ evolution, *RSC Adv.* 3 (2013) 25902–25907.
- K. Sun, S. Shen, J.S. Cheung, X. Pang, N. Park, J. Zhou, Y. Hu, Z. Sun, S.Y. Noh, C.T. Riley, Si photoanode protected by a metal modified ITO layer with ultrathin NiO_x for solar water oxidation, *Phys. Chem. Chem. Phys.* 16 (2014) 4612–4625.
- H. Yoon, M.G. Mali, J.Y. Choi, M.-w. Kim, S.K. Choi, H. Park, S.S. Al-Deyab, M.T. Swihart, A.L. Yarin, S.S. Yoon, Nanotextured pillars of electrospayed bismuth vanadate for efficient photoelectrochemical water splitting, *Langmuir* 31 (2015) 3727–3737.
- M.-w. Kim, B. Joshi, H. Yoon, T.Y. Ohm, K. Kim, S.S. Al-Deyab, S.S. Yoon, Electrospayed copper hexaaxodivanadate (CuV₂O₆) and pyrovanadate (Cu₂V₂O₇) photoanodes for efficient solar water splitting, *J. Alloys. Compd.* 708 (2017) 444–450.
- R. Tsybukh, A Comparative Study of Platinum Nanodeposits on HOPG (0001), MnO (100) and MnOx/MnO (100) Surfaces by STM and AFM After Heat Treatment in UHV, O₂, CO and H₂, (2010).
- K.L. Pickrahn, S.W. Park, Y. Gorlin, H.-B.-R. Lee, T.F. Jaramillo, S.F. Bent, Active MnOx electrocatalysts prepared by atomic layer deposition for oxygen evolution and oxygen reduction reactions, *Adv. Energy Mater.* 2 (2012) 1269–1277.
- W.H. Shin, T.H. Hwang, Y.S. Huh, J.W. Choi, Electrochemically controlled nanopore and crystal structure evolution in zinc oxide nanorods, *J. Electrochem. Soc.* 159 (2012) A2143–A2147.
- H.K. Park, S.P. Hong, Y.R. Do, Vertical growth of ZnO nanorods prepared on an ITO-coated glass substrate by hydrothermal-electrochemical deposition, *J. Electrochem. Soc.* 159 (2012) D355–D361.
- A. Das, R.K. Sahoo, D.K. Mishra, S.K. Singh, R.S. Mane, K.H. Kim, Thermal plasma-inspired synthesis of ZnO_{1-x}Mn_x dilute magnetic semiconductors for enhanced visible light photocatalysis, *Appl. Surf. Sci.* 467 (2019) 1059–1069.
- M. Qiu, Z. Chen, Z. Yang, W. Li, Y. Tian, W. Zhang, Y. Xu, H. Cheng, ZnMn₂O₄ nanorods: an effective Fenton-like heterogeneous catalyst with $t_{2g}^3e_g^1$ electronic configuration, *Catal. Sci. Technol.* 8 (2018) 2557–2566.
- H. Peng, T. Wu, Nonvolatile resistive switching in spin ZnMn₂O₄ and ilmenite ZnMnO₃, *Appl. Phys. Lett.* 95 (2009) 152106.
- L.-X. Zhang, Y.-L. Wang, H.-F. Jiu, H.-y. Qiu, H.-y. Wang, Hollow core-shell ZnMn₂O₄ microspheres as a high-performance anode material for lithium-ion batteries, *Ceram. Int.* 41 (2015) 9655–9661.
- D. Wu, J. Ma, Y. Bao, W. Cui, T. Hu, J. Yang, Y. Bai, Fabrication of porous Ag/TiO₂/Au coatings with excellent multipactor suppression, *Sci. Rep.* 7 (2017) 43749.
- M. Shaban, J. Poostforooshan, A.P. Weber, Surface-initiated polymerization on unmodified inorganic semiconductor nanoparticles via surfactant-free aerosol-based synthesis toward core-shell nanohybrids with a tunable shell thickness, *J. Mater. Chem. A Mater.* 5 (2017) 18651–18663.
- S. Zhao, J. Huang, Y. Liu, J. Shen, H. Wang, X. Yang, Y. Zhu, C. Li, Multimetallic Ni–Mo/Cu nanowires as nonprecious and efficient full water splitting catalyst, *J. Mater. Chem. A Mater.* 5 (2017) 4207–4214.
- L. Steier, J. Luo, M. Schreier, M.T. Mayer, T. Sajavaara, M. Grätzel, Low-temperature atomic layer deposition of crystalline and photoactive ultrathin hematite films for solar water splitting, *ACS Nano* 9 (2015) 11775–11783.
- D. Liang, C. Lian, Q. Xu, M. Liu, H. Liu, H. Jiang, C. Li, Interfacial Charge polarization in Co₂P₂O₇@N, P Co-doped carbon nanocages as mott-schottky electrocatalysts for accelerating oxygen evolution reaction, *Appl. Catal. B* (2019) 118417.
- N. Mao, Investigating the heterojunction between ZnO/Fe₂O₃ and gC_3N_4 for an enhanced photocatalytic H₂ production under visible-light irradiation, *Sci. Rep.* 9 (2019) 1–9.
- T. Mahardika, N.A. Putri, A.E. Putri, V. Fauzia, L. Roza, I. Sugihartono, Y. Herhani, Rapid and low temperature synthesis of Ag nanoparticles on the ZnO nanorods for photocatalytic activity improvement, *Results Phys.* 13 (2019) 102209.
- C. Li, Z. Luo, T. Wang, J. Gong, Surface, bulk, and interface: rational design of hematite architecture toward efficient photo-electrochemical water splitting, *Adv. Mater.* 30 (2018) 1707502.

- [56] D.W. Kim, S.C. Riha, E.J. DeMarco, A.B. Martinson, O.K. Farha, J.T. Hupp, Greenlighting photoelectrochemical oxidation of water by iron oxide, *ACS Nano* 8 (2014) 12199–12207.
- [57] F. Xu, J. Chen, S. Kalytchuk, L. Chu, Y. Shao, D. Kong, K.-H. Chu, P.H.-L. Sit, W.Y. Teoh, Supported gold clusters as effective and reusable photocatalysts for the abatement of endocrine-disrupting chemicals under visible light, *J. Catal.* 354 (2017) 1–12.
- [58] L. Li, S. Zhang, H. Zhao, A low cost universal photoelectrochemical detector for organic compounds based on photoelectrocatalytic oxidation at a nanostructured TiO₂ photoanode, *J. Electroanal. Chem.* 656 (2011) 211–217.